Springer

KSME

Journal of Mechanical Science and Technology 28 (11) (2014) 4527~4537
www.springerlink.com/content/1738-494x
DOI 10.1007/s12206-014-1020-7

# Experimental and numerical research on cavitating flows around axisymmetric bodies †

Wei Haipeng[1,*], Fu Song[1], Wu Qin[2], Huang Biao[2] and Wang Guoyu[2]

[1]*School of Aerospace Engineering, Tsinghua University, Beijing, 100084, China*
[2]*School of Mechanical Engineering, Beijing Institute of Technology, Beijing 100081, China*

(Manuscript Received March 16, 2014; Revised July 3, 2014; Accepted July 18, 2014)

**Abstract**

We investigated the cavitating flows around different axisymmetric bodies based on experiments and numerical simulation. In the numerical simulation, the multiphase Reynolds averaged Navier Stokes equations (RANS) were solved via the commercial computational fluid dynamics code CFX. The modified $k$-$\omega$SST turbulence model was used along with the transport equation-based cavitation model. In the experiments, a high-speed video technique was used to observe the unsteady cavitating flow patterns, and the dynamic force measurement system was used to measure the hydrodynamics of the axisymmetric bodies under different cavitation conditions. Results are shown for the hemisphere bodies, conical bodies and blunt bodies. Reasonable agreements were obtained between the computational and experimental results. The results show that for the hemispherical body, the cavity consists of quasi-steady transparent region and unsteady foggy water-vapor mixture region, which contains small-scale vortices and is dominated by bubble clusters, causing irregular disturbances at the cavity interfaces. The curvature at the front of the conical body is larger, resulting in that the flow separates at the shoulder of the axisymmetric body. The cavity stretches downstream and reaches to a fixed cavity length and shape. For blunt bodies, the incipient cavitation number is larger than that for the hemispherical body. A large cloud cavity is formed at the shoulder of the blunt body in the cores of vortices in high shear separation regions and the re-entrant jet does not significantly interact with the cavity interface when it moves upstream. As to the dynamic characteristics of unsteady cavitating flows around the axisymmetric bodies, the pulsation frequency for the hemispherical body is larger than that for the blunt body. For the hemispherical body, the pulsation is mainly caused by the high-frequency, small-scale shedding at the rear end of the cavity, while for the blunt body, the main factor for the pulsation frequency is the periodically shedding of large-scale vortex cavities.

*Keywords*: Blunt body; Cavitating flows; Conical body; Hemisphere body

## 1. Introduction

Because of its effect on stability, maneuverability and range, the hydrodynamic force of an underwater vehicle, such as underwater rocket, torpedo or submarine, is crucial for the general design of the ballistic trajectory and control system. Cavitation on the underwater vehicle, which involves complex phase-change dynamics, large density ratio between phases and multiple time scales [1-7], can lead to many problems such as pressure pulsation, sudden change in loads and vibration. For this reason, it is of critical importance to predict the development and evolution of cavitation, as well as the resultant impact on the performance accurately.

Several experimental investigations have been conducted in an attempt to develop a better understanding of the transition and cavitation processes on revolution bodies. Rouse and McNown [8] carried out a series of experiments on natural cavitation about axisymmetric bodies. Measurements were made across a range of cavitation number and have been applied in a wide range of investigations. Arakeri et al. [9] made a large number of studies on the cavitating flow around axisymmetric bodies and found various types of cavities. Ceccio et al. [10] recorded the volume fluctuations of the cavities by measuring the local fluid impedance near the cavitating surface. The results revealed that the cavities fluctuated at specific frequencies associated with the oscillations of the cavity closure region. Liu et al. [11] conducted experiments with different cavitation numbers, angles of attack for different body shapes. They obtained the incipient cavitation number for the blunt body at different angle of attack and established the calculation formulas for the geometry parameters of cavity characteristics. With the numerical technique and computing power advancing, computational fluid dynamics (CFD) has become a promising tool for exploring the cavitating flows around axisymmetric bodies [12-14]. Historically, most efforts

*Corresponding author. Tel.: +86 13466503161, Fax.: +86 010 88521759
E-mail address: weilhaipeng1982@163.com
† Recommended by Associate Editor Gihun Son

to model large cavities relied on the potential flow methods for the fluid flow while the bubble shapes and closure conditions were specified [15]. Recently, to further analyze these flows, more general CFD approaches have been developed. Kunz [16] established an implicit algorithm for the computation of viscous two-phase flows based on the multiphase Navier-Stokes equations, which is applied to numbers of high density ratio sheet-cavitating and super-cavitating flows. The results verified that the tool was able to analyze steady-state and transient sheet-cavitating and super-cavitating flows accurately. Lindau et al. [17] presented a computational model capable of capturing fully compressible multiphase flow with energy equations considered. The results demonstrated the effectiveness of the preconditioning form and the ability of the computational model to predict complex, engineering level, flow fields.

Our objective was to evaluate the predictive capability of the numerical method for the simulations of cavitating flows around the revolution bodies and to improve the understanding of flow structures and hydrodynamic characteristics of the cavitating flow around the axisymmetric bodies. The experimental setup is first introduced and the numerical methods are presented. The $k$-$\omega$ SST turbulence model is summarized, followed by the density correction model for the turbulent viscosity modification and the popular transport-based cavitation model. Then the steady natural cavitation and unsteady sheet/cloud cavitation on axisymmetric bodies are analyzed with combined experimental and numerical investigation.

## 2. Experimental setup

The experiments were in a closed-loop cavita-tion tunnel, shown in Fig. 1. An axial flow pump is located 5 m below the test section to drive the flow in the tunnel. Upstream of the test section, the tank with volume of 5 $m^3$ is placed to separate the undesired free stream bubbles. The pressure in the tunnel is controlled by the vacuum pump which is connected to the top of the tank. In addition, a straightening vane and a corner vane between the tank and the test section are used to reduce the turbulence level of the flow. The experiment conditions were maintained within 2% uncertainty on the flow velocity and the upstream pressure, which were measured by the electromagnetic flowmeter (with 0.5% uncertainty) and the pressure transducer (with 0.25% uncertainty) respectively. For a further detailed description see Ref. [18].

Cavitation phenomena were recorded by a high-speed digital camera (HG-LE, by Redlake), up to a rate of $10^5$ fps, as illustrated in Fig. 2. To maintain desirable spatial resolutions, a rate of 1000 fps was used in this study, with three light sources illuminating the flow field from different directions. The pictures were captured and transmitted to the computer for post processing.

The dynamic force measurement system, as shown in Fig. 3, consisted of a dynamic strain gauge (SDY2102), a charge amplifier and a data acquisition system (DASP). The sampling

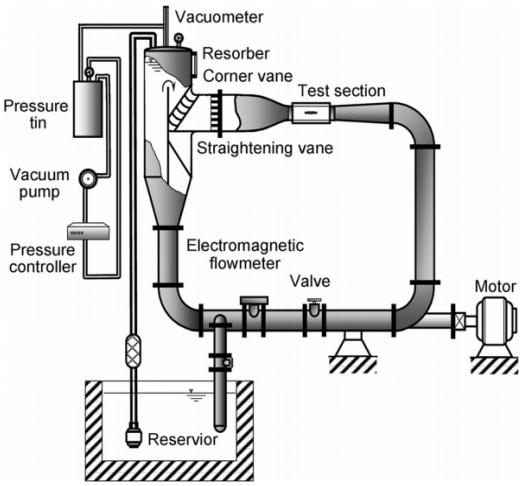


Fig. 1. Schematic of the cavitation tunnel.

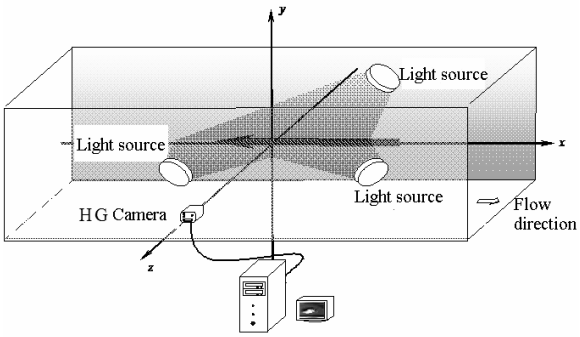


Fig. 2. Layout of the experimental setup.

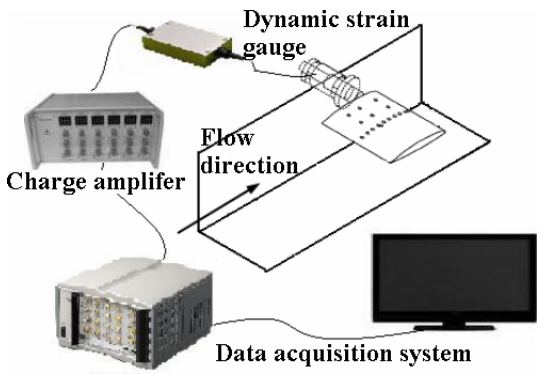


Fig. 3. Dynamic measurement system.

frequency of the dynamic strain gauge was 1 kHz.

## 3. Governing equations and numerical techniques

### *3.1 Continuity and momentum equations*

The Navier-Stokes equations in their conservative form governing a Newtonian fluid in the Cartesian coordinates [19] are presented below:

$$\frac{\partial \rho_{\mathrm{m}}}{\partial t}+\frac{\partial(\rho_{\mathrm{m}} u_j)}{\partial x_j}=0, \tag{1}$$

$$\frac{\partial(\rho_{\mathrm{m}} u_i)}{\partial t}+\frac{\partial(\rho_m u_i u_j)}{\partial x_j}=-\frac{\partial p}{\partial x_i} + \frac{\partial}{\partial x_j}\left[(\mu_{\mathrm{m}}+\mu_{\mathrm{t}})\left(\frac{\partial u_i}{\partial x_j}+\frac{\partial u_j}{\partial x_i}-\frac{2}{3}\frac{\partial u_k}{\partial x_k}\delta_{ij}\right)\right], \tag{2}$$

$$\frac{\partial \rho_{\mathrm{l}}\alpha_{\mathrm{l}}}{\partial t}+\frac{\partial(\rho_{\mathrm{l}}\alpha_{\mathrm{l}} u_j)}{\partial x_j}=\dot{m}^{+}+\dot{m}^{-}, \tag{3}$$

$$\rho_{\mathrm{m}}=\rho_{\mathrm{l}}\alpha_{\mathrm{l}}+\rho_{\mathrm{v}}\alpha_{\mathrm{v}}, \tag{4}$$

$$\mu_{\mathrm{m}}=\mu_{\mathrm{l}}\alpha_{\mathrm{l}}+\mu_{\mathrm{v}}\alpha_{\mathrm{v}}, \tag{5}$$

where $\rho_m$ is the mixture density, $u$ is the velocity, $p$ is the pressure, $\mu_m$ is the mixture laminar viscosity and $\mu_t$ is the turbulent viscosity. The subscripts $i$, $j$, $k$ represent the axes directions. The source term $\dot{m}^{+}$, and the sink term $\dot{m}^{-}$ in Eq. (3) are the condensation and evaporation rates, respectively.

### 3.2 Turbulence model and local compressibility correction

The numerical results are from the commercial CFD code, CFX, to solve the URANS equations. The *k-ω* SST turbulence model was applied, which combines the advantages of the standard *k-ε* and *k-ω* models [20]. The *k-ω* SST turbulence model was validated for good prediction of the boundary layer detachment characteristics [21].

$$\frac{\partial(\rho k)}{\partial t}+\frac{\partial(\rho U_j k)}{\partial x_j}=P_k-D_k+\frac{\partial}{\partial x_i}\left[(\mu+\frac{\mu_t}{\sigma_k})\frac{\partial k}{\partial x_i}\right] \tag{6}$$

$$\frac{\partial(\rho\omega)}{\partial t}+\frac{\partial(\rho U_j \omega)}{\partial x_j}=C_\omega P_\omega-\beta_\omega\rho\omega^2+\frac{\partial}{\partial x_i}\left[(\mu+\frac{\mu_t}{\sigma_k})\frac{\partial \omega}{\partial x_i}\right]+2\rho(1-F_1)\sigma_{\omega 2}\frac{1}{\omega}\frac{\partial k}{\partial x_i}\frac{\partial \omega}{\partial x_i}. \tag{7}$$

The eddy viscosity is confirmed as:

$$v_t=\frac{\rho a_1 k}{\max(a_1\omega;\ SF_2)}, \tag{8}$$

where, $P_k$ and $P_\omega$ are production terms, $D_k$ is the destruction term, $F_1$ and $F_2$ are blending functions, $S$ is the absolute value of the strain.

To avoid over-prediction of the turbulent eddy viscosity and turbulent stress by the original RANS models, the influence of the local compressibility effects on turbulent closure models were taken into consideration in the present work. Based on the local liquid volume fraction $\alpha_l$ by substituting $\mu_t$, the turbulent viscosity in Eqs. (6) and (7) was reduced with $\mu_{t\_mod}$:

$$f(n)=\frac{\rho_{\mathrm{v}}+(1-\alpha_{\mathrm{v}})^n(\rho_{\mathrm{l}}-\rho_{\mathrm{v}})}{\rho_{\mathrm{v}}+(1-\alpha_{\mathrm{v}})(\rho_{\mathrm{l}}-\rho_{\mathrm{v}})},\ \mu_{\mathrm{t\_mod}}=\mu_{\mathrm{t}}f(n). \tag{9}$$

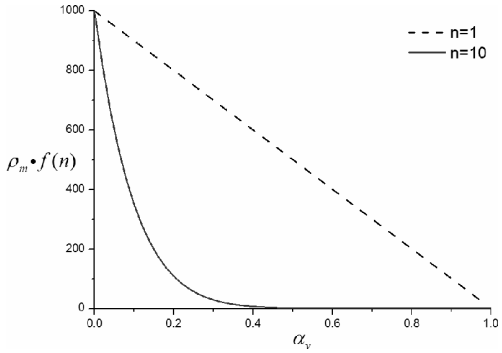


Fig. 4. Variation of the modified mixture density for $n$ = 1 and $n$ = 10.

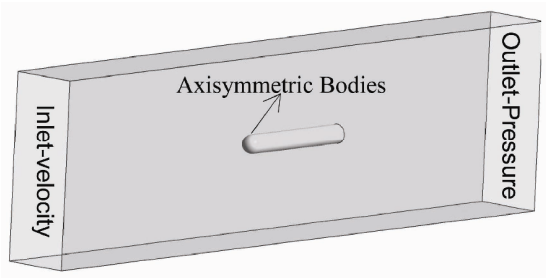


Fig. 5. Computational domain and boundary conditions.

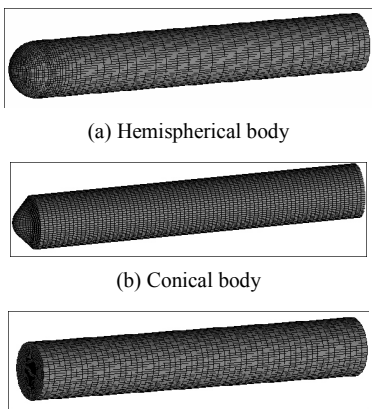

(a) Hemispherical body

(b) Conical body

(c) Blunt body

Fig. 6. Mesh distributions.

The variation of the modified mixture density $\rho_m$**f(n)* with the water vapor volume fraction $\alpha_v$ for $n$ = 1 and $n$ = 10 is shown in Fig. 4. According to Ref. [22], $n$ = 10 was chosen to better simulate the re-entrant jet and vapor shedding process in this paper.

### 3.3 Cavitation model

The cavitation model used was proposed by Merkle [23]. It assumes that the evaporation and condensation terms are proportional to the difference between the local pressure and the vapor pressure. The mass fraction form of the evaporation and condensation terms can be written as:

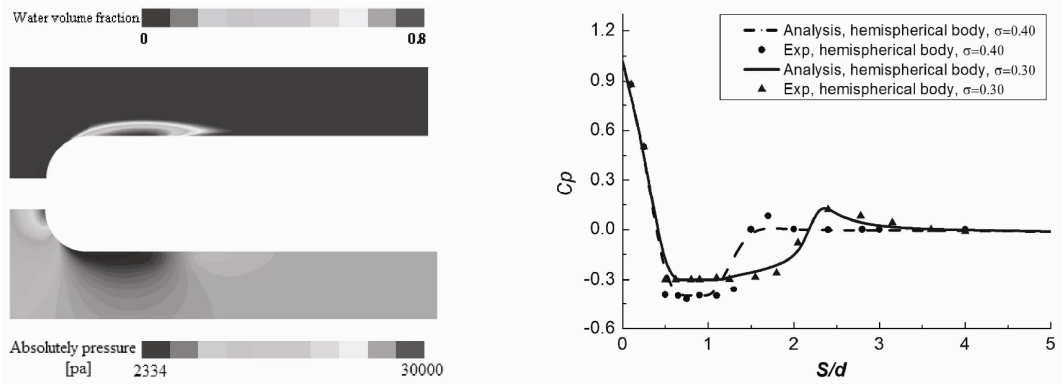


(a) Hemispherical, σ = 0.30

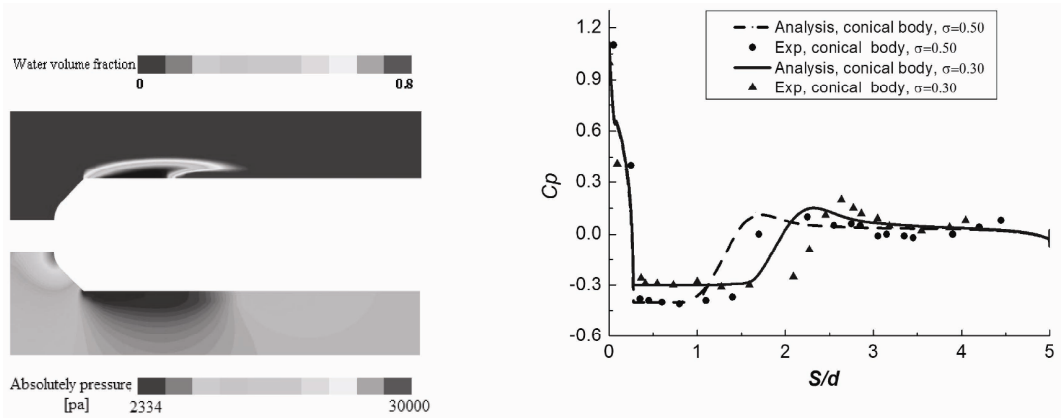


(b) Conical, σ = 0.30

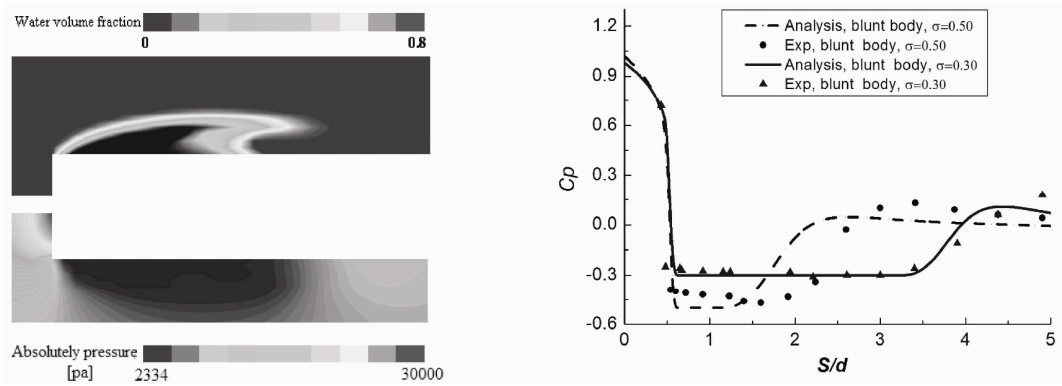


(c) Blunt, σ = 0.30

Fig. 7. The predicted vapor volume fraction, pressure distribution and the measured values from Ref. [5] around revolution bodies.

$$\dot{m}^{-} = \frac{C_{m\_dest}\rho_l \rho_l MIN\left(p - p_v, 0\right)(1-\alpha_v)}{(0.50\rho_l U_\infty^2)\rho_v t_\infty}, p < p_v \quad (10)$$

$$\dot{m}^{+} = \frac{C_{m\_prod}\rho_l MAX\left(p - p_v, 0\right)\alpha_v}{(0.50\rho_l U_\infty^2)t_\infty}, p > p_v\ , \quad (11)$$

where the empirical factors $C_{m\_dest}$ and $C_{m\_prod}$ are, respectively, the destruction and the production coefficients. In this work, $C_{m\_dest}$ = 1.0 and $C_{m\_prod}$ = 80, which is accordance with Ref. [24]. The mean time scale is defined as $t_\infty = d/U_\infty$.

### *3.4 Numerical setup and description*

The computational domain and boundary conditions for the axisymmetric bodies are shown in Fig. 5, which is consistent with the experimental setup. The diameter of the axisymmetric body is $d$ = 20 mm and the length is $L$ = 7.5$d$. The conical angle is $\theta$ = 90°. The computational domain has an extent of 15$d$ upstream and 20$d$ downstream to simulate the near-infinite boundary at both the inlet and the outlet. The O-type mesh was adopted and mesh refinements were also performed

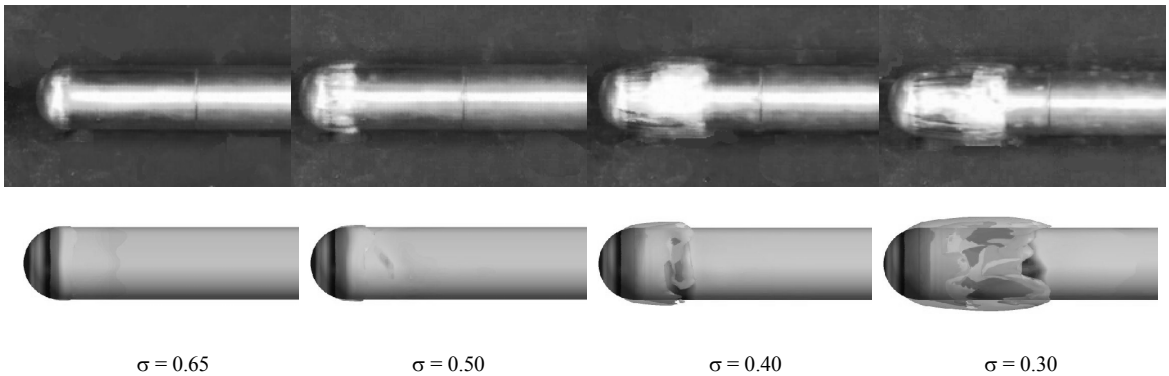

σ = 0.65 σ = 0.50 σ = 0.40 σ = 0.30

(a) Hemispherical body

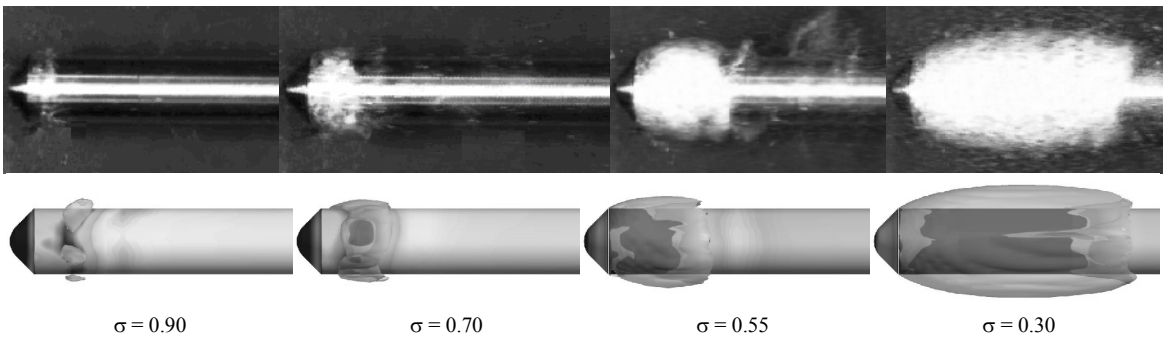

σ = 0.90 σ = 0.70 σ = 0.55 σ = 0.30

(b) Conical body

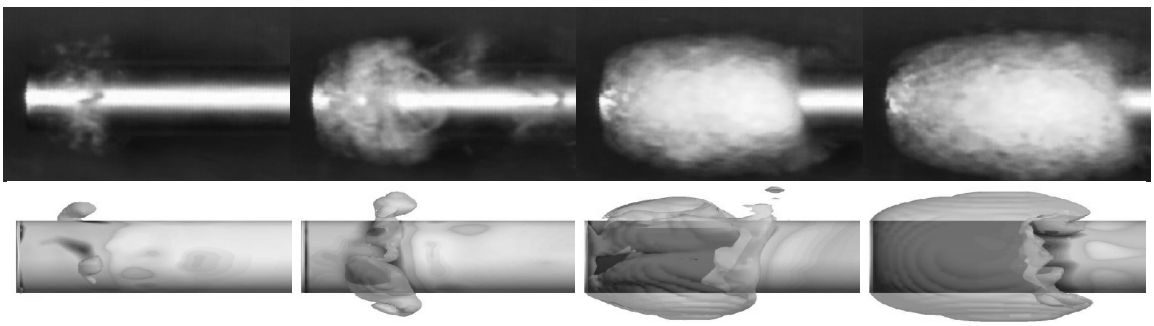

σ = 0.90 σ = 0.75 σ = 0.65 σ = 0.55

(c) Blunt body

Fig. 8. The cavity shapes for the axisymmetric bodies with different headforms.

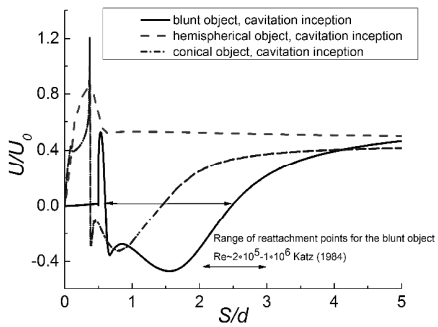


Fig. 9. The predicted flow reattachment for the axisymmetric bodies with different headforms.

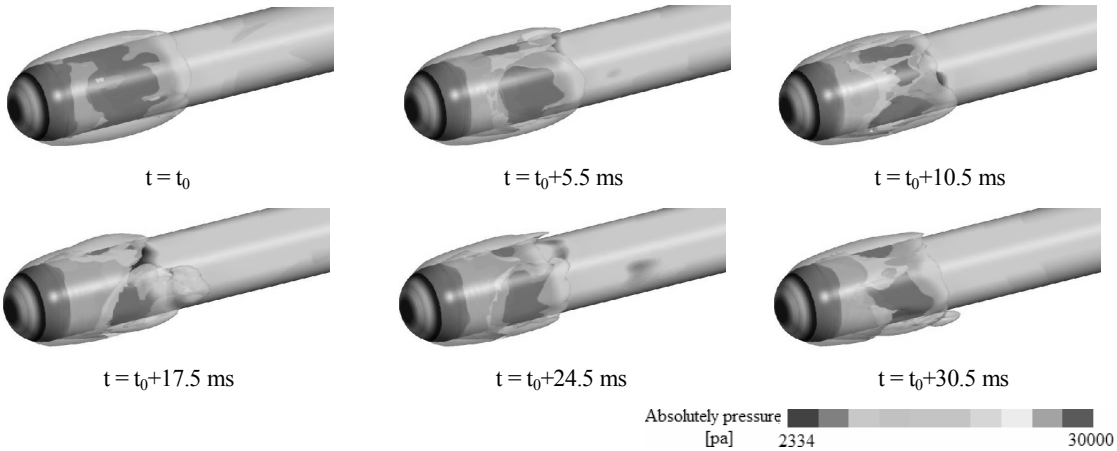


(a) Time evolution of the 3D cavity shapes

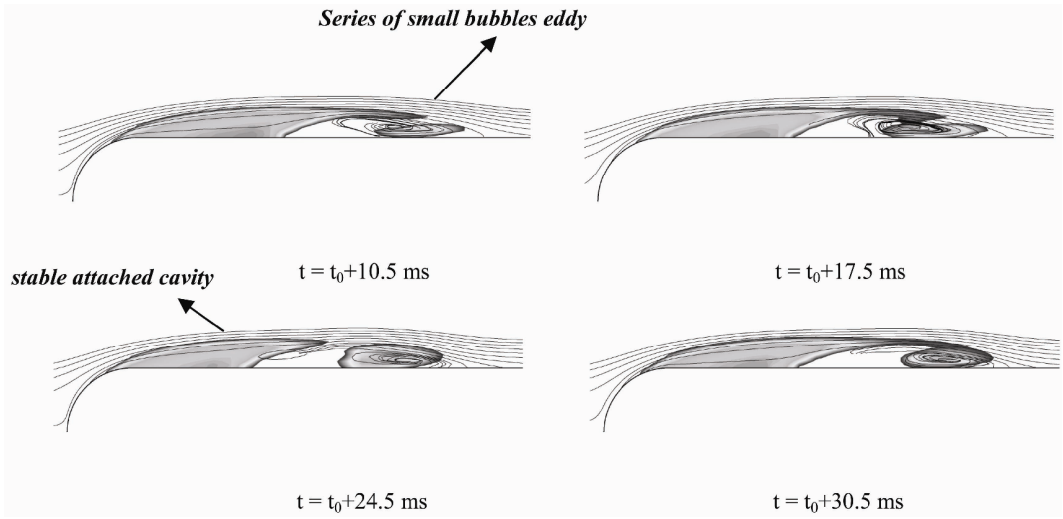


(b) Time evolution of the 2D cavity shapes

Fig. 10. Cavity shapes and unsteady shedding characteristics for hemispherical body ($\sigma = 0.3$).

at the head of the axisymmetric bodies. The total mesh was composed of 135000 structured elements with $y^+ = yu_\tau/\nu \approx 1$, where $y$ is the thickness of the first cell from the body surface, and $u_\tau$ is the wall frictional velocity. The mesh distribution near the surface is shown in Fig. 6.

All the results shown in this paper are subject to a free stream velocity of $U_\infty = 6.8$ m/s, yielding a Reynolds number of $Re = U_\infty c/\nu_l = 1.36\times10^5$. The outlet pressure varies according to the cavitation number $\sigma = (p_\infty - p_v)/(0.5\rho_l V_\infty^2)$, where $p_\infty$ represents the tunnel pressure. Based on the experimentally measurement, the turbulent intensity at the inlet boundary is set as 2%. To avoid any vapor fraction at the initial time step, all simulations were initialized with a steady-state calculation with fully wetted models. According to Refs. [25-26], the second-order backward Euler algorithm was chosen for the time integrator scheme and the second-order upwind scheme was used to compute the spatial derivatives. Further mesh convergence and time discretization were studied in Ref. [21].

## 4. Results and discussion

### *4.1 The validation of the numerical models*

To validate the numerical model, results are shown for the axisymmetric bodies. Fig. 7 shows the predicted vapor volume fraction and pressure distribution obtained for the hemispherical, conical and blunt bodies, as well as the measured values from Ref. [5]. In general, reasonable agreement is observed between the computations and measurement. For all the cases, the presence of the bubble manifests itself as the decreases in magnitude, flattening and lengthening of the minimum pressure along the surface. On each of the three figures, the nearly constant pressure region with $C_p = -\sigma$ corresponds to the partial sheet cavity attached at the forebody, as shown in left side of Fig. 7, followed by a sudden pressure jump at the cavity closure region due to the local stagnation associated with free-stream liquid flowing over the aft end of the bubble and transition back to sub-cavitating flow.

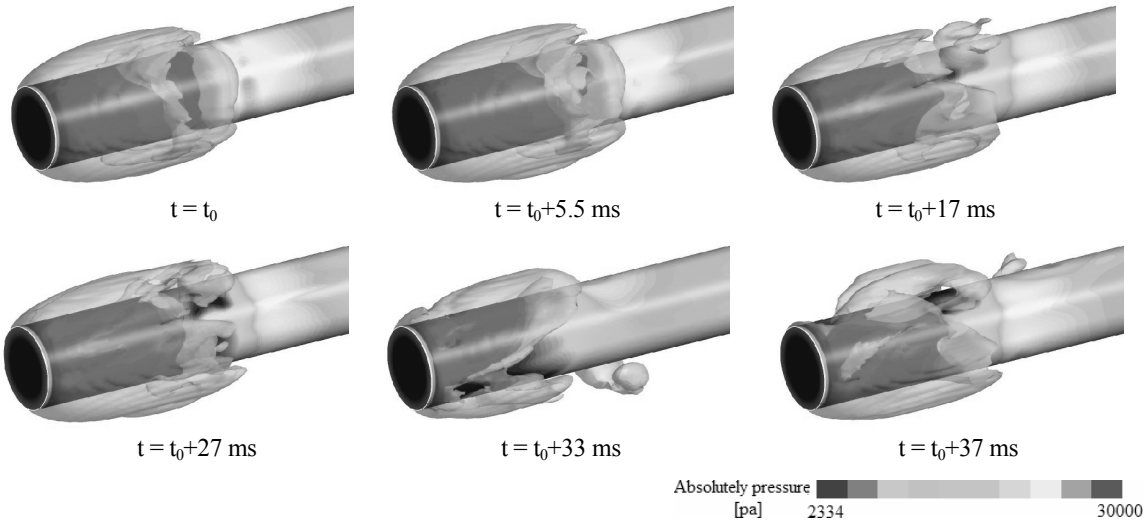


(a) Time evolution of the 3D cavity shapes

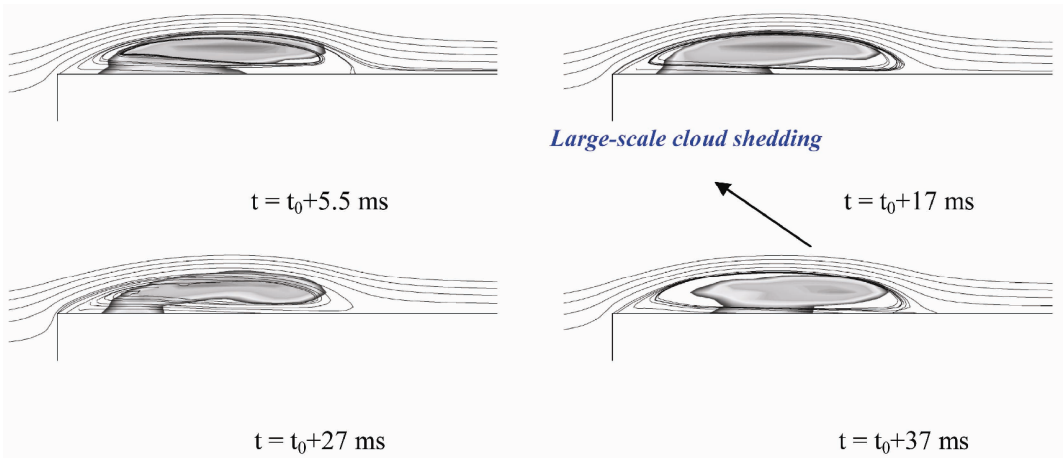


(b) Time evolution of the 2D cavity shapes

Fig. 11. Cavity shapes and unsteady shedding characteristics for blunt body ($\sigma = 0.50$).

### *4.2 Unsteady flow structures around axisymmetric bodies*

To further investigate the effects of the headforms on the cavitating flows, results are shown in this section for the unsteady flow structures around the hemispherical, blunt and conical bodies.

Fig. 8 shows the measured and predicted typical cavity shapes at different cavitation numbers. For the hemispherical body shown in Fig. 8(a), an incipient cavity is formed at the front of the axisymmetric body when $\sigma = 0.65$; as the cavitation number decreases to about 0.5, the cavity is drawn out and attached like fingers. With further decreasing of the cavitation number, the cavity develops and covers the whole forebody circumferentially; when the cavity can be divided into two parts obviously: one is the transparent region with high vapor volume fraction, and the other is the unsteady foggy water-vapor mixture region, which contains small scale vortices and is dominated by bubble clusters, causing irregularly disturbances at the cavity interfaces.

As shown in Fig. 8(b), compared to the hemispherical body, the curvature at the front of the conical body is larger, resulting in flow separation at the shoulder of the axisymmetric body. With the decreases of the cavitation number, the cavitation area increases gradually and the separation point is moving forward. When $\sigma = 0.50$, obvious cloud cavitation with an ellipsoidal cavity can be observed, which is filled with the water-vapor mixture. When the cavitation number decreases to 0.3, the cloud cavitation develops to a stable stage. The cavity has stretched downstream and reached to a fixed cavity length and shape.

The cavity shapes with the blunt bodies are different from those with hemispherical and conical bodies, because of the different boundary layer flow characteristics. For the blunt bodies shown in Fig. 8(c), the incipient cavitation number is larger than that for the hemispherical body. When $\sigma = 0.90$, flow separates at the sharp corner of the body and continuous

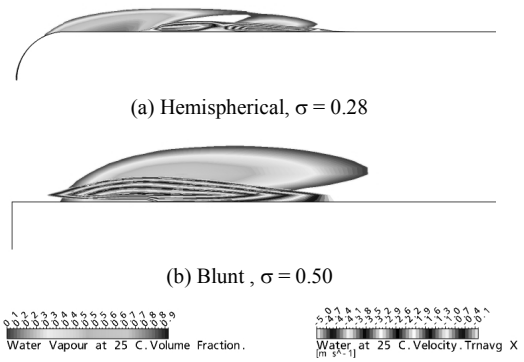


Fig. 12. The cavity shapes and the averaged velocity distribution for the hemispherical and blunt bodies during the re-entrant jet stage.

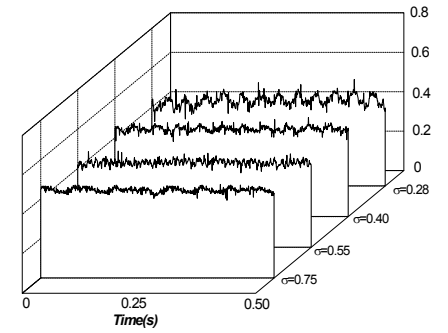


(a) Hemispherical body

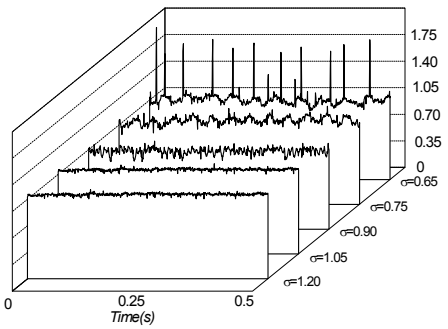


(b) Blunt body

Fig. 13. The evolution of wavelet transformed drag coefficients with time.

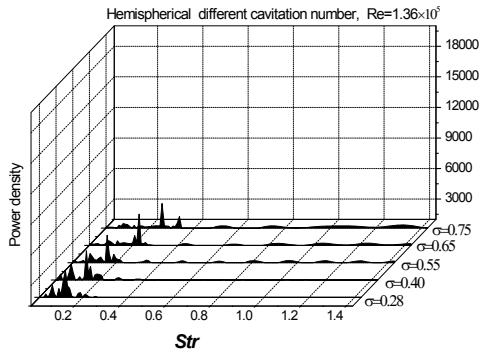


(a) Hemispherical body

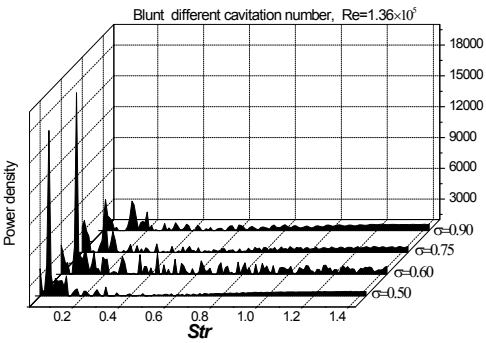


(b) Blunt body

Fig. 14. The spectrum analysis of resistance signals.

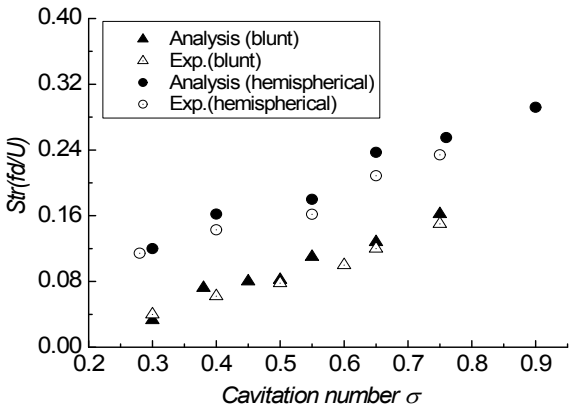


Fig. 15. The evolution of Strouhal number *Str* with cavitation number σ.

cavitation bubble vortex structures can be observed. Cavities are formed in the cores of vortices in high shear separation regions.

Fig. 9 compares the different locations of the flow separation and reattachment points around the axisymmetric bodies. For the blunt body, the flow reattachment can be observed and in accordance with the experimental results by Katz [27]. The reverse flow region for the blunt and conical body expands to be at a distance of 2.5*d* and 1.5*d* to the head of the body respectively, while for the hemispherical body, there is no obvious flow separation and reattachment.

To further investigate the unsteady characteristics of the cavitating flow around the axisymmetric bodies, Fig. 10 shows the typical time evolution of cavity for hemispherical bodies, when the cavitation number is 0.3. From Fig. 10, it has been widely observed that the sheet cavitation is stable in a quasi-steady sense, with a stable cavity attached at the shoulder of the axisymmetric body. While at the rear end of the sheet cavity, series of small-scale bubble vortices, as well as the small vapor structures, are quasi-periodically forming, fluctuating and shedding.

Fig. 11 contains a series of snapshots of the vapor volume fraction field from an unsteady model computation of flow over a blunt body at cavitation numbers 0.50. For blunt bodies,

flow separates strongly at the shoulder of the body due to the sudden change of the curvature, forming a large-scale vortex, where the cavitation occurs and an ellipsoidal cavity is formed. As the cavity develops to its maximum extent, the separated vortex gathers and strengthens at the rear region of the cavity, resulting in strongly reverse flow near the surface. The depression regions occur at the end of the cavity and fluctuates circumferentially so that the cavities break partially, and finally the large-scale cloud cavity is shedding downstream as a whole periodically.

Re-entrant jet instability is often attributed to the cavity de stabilization and transition to unsteady cavitation. Fig. 12 shows the vapor volume fraction as well as the averaged velocity distribution for the hemispherical and blunt bodies during the re-entrant jet stage. In the case of a relatively thin cavity for the unsteady cavitating flows around the hemispherical body, because of the smallness of the cavity thickness and consequently of the closeness of the cavity interface and the boundary of the re-entrant jet, there exists a strong interaction between the cavity interface and the re-entrant jet, all along its upstream movement. The thin vapor layer between the cavity interface and the re-entrant jet breaks at many points due to the small scale instabilities. As for the flow around the blunt body, the re-entrant jet does not significantly interact with the cavity interface when it moves upstream. The interaction is limited at the instant the re-entrant jet reaches the leading edge of the cavity and cuts the cavity interface. Contrary to many small vapor structures around the hemispherical body, a large cloud cavity is formed at the shoulder of the blunt body. In conclusion, the differences between the cavitating flow structures lead to the discrepancy of the unsteady cavity shedding characteristics of the hemispherical body and blunt body.

### *4.3 Dynamic characteristics of unsteady cavitating flows on revolution body*

Based on the experimental results for the hemispherical and blunt bodies, Fig. 12 shows the time evolution of wavelet transformed drag coefficients for different cavitation numbers. When the cavitation number is larger than the incipient cavitation numbers, irregular small-scale fluctuations of the drag coefficient can be observed, and there no obvious cavitation occurs in the flow field. With the cavitation number decreasing, the fluctuation amplitudes of the drag coefficients increase with an obvious periodicity. Fig. 13 shows the spectrum analysis of resistance signals. The characteristics frequency is low and the fluctuation characteristics vary with different headforms of the axisymmetric bodies, which is due to the variation of the unsteady cavities. When the cavitation number is about 0.65, large-scale cavities shed downstream periodically in the cavitating flow around a blunt body and the fluctuation amplitude and power spectral density is much larger than that of other conditions. The low characteristic frequency is corresponding to the inherent fluctuation frequencies of the cavitating flow. In general, the fluctuations of the drag signals of the blunt body are much more significant than that of the hemispherical body.

Fig. 14 shows the evolution of Strouhal number *Str* with cavitation number σ, where the Strouhal number is defined as $Str = fD_n/U_\infty$, $f$ is the pulsation frequency of the bodies, $D_n$ is the diameter of the axisymmetric body. Reasonable agreement is obtained between the numerical and experimental results. In general, the variation of Strouhal number *Str* is mainly caused by the cavities shedding. The pulsation frequency for the hemispherical body is larger than that for the blunt body. This is because, for the hemispherical body, the pulsation is mainly caused by the high-frequency, small-scale shedding at the rear end of the cavity, while for the blunt body, the main factor for the pulsation frequency is the periodic shedding of the large-scale vortex cavities.

## 5. Conclusions

Numerical modeling is studied for the prediction of cavitation flows around axisymmetric bodies. The calculations are performed by solving the multiphase Reynolds averaged Navier Stokes equations (RANS) via the commercial CFD code CFX. The modified $k$-$\omega$ SST turbulence model is used along with the transport equation-based cavitation model. The predicted and measured cavity shapes and hydrodynamic coefficients are also compared. The general conclusions of this paper are as follows:

(1) In general, reasonable agreements are obtained between the computations and measurements for the hemisphere body, conical body and blunt body. The nearly constant pressure region with $Cp = -\sigma$ corresponds to the partial sheet cavity attached around the body, followed by a sudden pressure jump at the cavity closure region due to the local stagnation associated with free-stream liquid flowing over the aft end of the bubble and transition back to sub-cavitating flow.

(2) For the hemispherical body, the cavity consists of quasi-steady transparent region and unsteady foggy water-vapor mixture region, which contains small scale vortices and is dominated by bubble clusters, causing irregular disturbances at the cavity interfaces. There exists a strong interaction between the cavity interface and the re-entrant jet, all along its upstream movement. Compared to the hemispherical body, the curvature at the front of the conical body is larger resulting in that flow separates at the shoulder of the axisymmetric body. With the decreases of the cavitation number, the cavitation area increases gradually and the separation point is moving forward. The cavity has stretched downstream and reached to a fixed cavity length and shape. For blunt bodies, the incipient cavitation number is larger than that for the hemispherical body. Contrary to many small vapor structures around the hemispherical body, a large cloud cavity is formed at the shoulder of the blunt body in the cores of vortices in high shear separation regions, and the re-entrant jet does not significantly interact with the cavity interface when it moves upstream. The differences between the cavitating flow struc-

tures lead to a discrepancy of the unsteady cavity shedding characteristics of the axisymmetric bodies.

(3) The pulsation frequency for the hemispherical body is larger than that for the blunt body. For the hemispherical body, the pulsation is mainly caused by the high-frequency, small-scale shedding at the rear region of the cavity, while for the blunt body, the main factor for the pulsation frequency is the periodic shedding of large-scale vortex cavities.

## Acknowledgment

This work was supported by the National Natural Science Foundation of China (Grant Nos. 51239005 and 51306020).

## Nomenclature

| | |
|---|---|
| $\rho_m$ | : Mixture density |
| $u$ | : Velocity |
| $p$ | : Pressure |
| $\mu_m$ | : Mixture laminar viscosity |
| $\mu_t$ | : Turbulent viscosity |
| $i, j, k$ | : Axes directions |
| $\dot{m}^+$ | : Condensation rate |
| $\dot{m}^-$ | : Evaporation rate |
| $P_k$, $P_\omega$ | : Production term |
| $D_k$ | : Destruction term |
| $F_1$, $F_2$ | : Blending function |
| $S$ | : Absolute value of the strain |
| $t_\infty$ | : Mean time scale |
| $d$ | : Diameter of the axisymmetric body |
| $U_\infty$ | : Free stream velocity |
| $Re$ | : Reynolds number |
| σ | : Cavitation number |

## References

[1] C. E. Brennen, *Cavitation and bubble dynamics*, Oxford Engineering & Sciences Series 44, Oxford University Press, New York, USA (1995).

[2] H. Sun, Numerical study of hydrofoil geometry effect on cavitating flow, *Journal of Mechanical Science and Technology*, 26 (8) (2012) 2535-2545.

[3] B. Ji, X. W. Luo, X. X. Peng, Y. L. Wu and H. Y. Xu, Numerical analysis of cavitation evolution and exited pressure fluctuation around a propeller in non-uniform wake, *International Journal of Multiphase Flow*, 43 (2012) 13-21.

[4] H. L. Liu, Y. Wang, D. X. Liu, S. Q. Yuan and J. Wang, Assessment of a turbulence model for numerical predictions of sheet-cavitating flows in centrifugal pumps, *Journal of Mechanical Science and Technology*, 27 (9) (2013) 2743-2750.

[5] S. Park, and S. H. Rhee, Numerical analysis of the three-dimensional cloud cavitating flow around a twisted hydrofoil, *Fluid Dynamics Research*, 45 (2013) 1-20.

[6] S. Park and S. H. Rhee, Computational analysis of turbulent supercavitating flow around a two-dimensional wedge-shaped cavitator geometry, *Computers and Fluids*, 70 (2012) 73-85.

[7] B. Ji, X. W. Luo, R. E. A. Arndt and Y. L. Wu, Numerical simulation of three dimensional cavitation shedding dynamics with special emphasis on cavitation-vortex interaction. *Ocean Engineering*, 87 (2014) 64-77.

[8] H. Rouse and J. S. McNown, *Cavitation and pressure distribution: head forms at zero angle of yaw*, Office of Naval Research, State University of lowa, Iowa City, USA (1948).

[9] V. H. Arakeri and A. J. Acosta, Viscous effects in the inception of cavitation on axisymmetric bodies, *Journal of Fluids Engineering*, 95 (4) (1973) 519-527.

[10] S. L. Ceccio and C. E. Brennen, Dynamics of attached cavities on bodies of revolution, *Journal of Fluids Engineering*, 114 (1992) 93-99.

[11] H. Liu, Q. Liu and T. Hu. An experimental study on fluctuating hydrodynamic loads on cavitating axisymmetric slender bodies, *Journal of Hydrodynamics*, 19 (6) (2004) 794-800.

[12] D. Kim, W.-G. Park and C.-M. Jung, Numerical simulation of cavitating flow past axisymmetric body, *International Journal of Naval Architecture and Ocean Engineering*, 4 (3) (2012) 256-266.

[13] Y. Kwack and S. H. Ko, Numerical analysis for supercavitating flows around axisymmetric cavitators, *International Journal of Naval Architecture and Ocean Engineering*, 5 (3) (2013) 323-332.

[14] J. W. Lindau, R. F. Kunz, D. A. Boger, D. R. Stinebring and H. J. Gibeling, High Reynolds number, unsteady, multiphase CFD modeling of cavitating flows, *ASME Journal of Fluid Engineering*, 124 (2002) 607-616.

[15] I. N. Kirchner, N. E. Fine and J. S. Uhlman, *Numerical modeling of supercavitating flows*, Anteon/Engineering Technology Center Mystic CT (2001).

[16] R. F. Kunz, D. A. Boger and D. R. Stinebring, A preconditioned Navier-Stokes method for two-phase flows with application to cavitation prediction, *AIAA paper*, AIAA-99-3329 (1999).

[17] J. W. Lindau, S. Venkateswaran, R. F. Kunz and C. L. Merkle, Computation of compressible multiphase flows, *41st Aerospace Sciences Meeting and Exhibit*, Reno, Nevada (2003).

[18] B. Huang and G. Y. Wang, Experimental and numerical investigation of unsteady cavitating flows through a 2D hydrofoil, *Science China-Technological Sciences*, 54 (7) (2011) 1801-1812.

[19] B. Launder and D. Spalding, The numerical computation of turbulent flows, *Computer Methods in Applied Mechanics and Engineering*, 3 (1974) 269-289.

[20] F. R. Menter, Improved two-equation $k$-$\omega$ turbulence models for aerodynamic flows, *NASA Technical Memorandum*, 103975, 34 (1993).

[21] A. Ducoin, J. A. Astolfi, F. Deniset and J.-F. Sigrist, Computational and experimental investigation of flow over a transient pitching hydrofoil, *European Journal of Mechanics/B Fluids*, 28 (2009) 728-743.

[22] O. Coutier-Delgosha, R. Fortes-Patella and J. Reboud, Evaluation of the turbulence model influence on the numeri-

cal simulations of unsteady cavitation, *Journal of Fluids Engineering*, 125 (1) (2003) 38-45.

[23] C. L. Merkle, J. Feng and P. E. O. Buelow, Computational modeling of the dynamics of sheet cavitation, *Proc. 3rd International Symposium on Cavitation*, Grenoble, France (1998).

[24] I. Senocak and W. Shyy, Evaluation of cavitation models for Navier-Stokes computations, *Proceedings of FEDSM 02, ASME 2002 Fluids Engineering Division Summer Meeting,* Montreal, Quebec, Canada (2002).

[25] B. Huang, A. Ducoin and Y. L. Young, Physical and numerical investigation of cavitating flows around a pitching hydrofoil, *Physics of Fluids*, 25 (2013) 102109.

[26] B. Huang, Y. L. Young, G. Y. Wang and W. Shyy, Combined experimental and computational investigation of unsteady structure of sheet/cloud cavitation, *Journal of Fluid Engineering*, 135 (2013) 071301.

[27] J. Katz, Cavitation phenomena within regions of flow separation, *Journal of Fluid Mechanics*, 140 (1984) 397-436.

**Wei Haipeng** received his B.S. degree from Harbin Institute of Technology and M.S. degree from China academy of Launch Vehicle Technology. He is a doctoral student of Aerospace School of Tsinghua University majoring fluid dynamics. His research field includes computation of multiphase flow and experimental study on cavitation. He is involved in developing new computational methods of multiphase flow and advanced observation technology of cavitation.